

# Shock compression-based equation of state for perfluorohexane

Anunay Prasanna,<sup>1,\*</sup> Guillaume T. Bokman,<sup>1</sup> Samuele Fiorini,<sup>1</sup>  
Armand Sieber,<sup>1</sup> Bratislav Lukić,<sup>2</sup> Daniel Foster,<sup>2</sup> and Outi Supponen<sup>1</sup>

<sup>1</sup>*Institute of Fluid Dynamics, D-MAVT, ETH Zürich, Switzerland*

<sup>2</sup>*European Synchrotron Radiation Facility, Grenoble, France*

(Dated: March 28, 2025)

Perfluorohexane is a biocompatible material that serves as a liquid core for acoustically-responsive agents in biomedical applications. Despite its relatively widespread usage, there is a lack of experimental data determining its thermodynamic properties. This challenges numerical simulations to predict the acoustic response of agents developed using this material. In this study, we employ the well-established method of shock compression of materials at relatively high pressures (100–400 MPa) to estimate a kinematic equation of state for perfluorohexane. We use multi-objective optimization to obtain the Noble-Abel Stiffened-Gas equation of state, which is suitable for hydrodynamic numerical simulations. We then apply the extrapolated equation of state to simulate shock-wave propagation within a perfluorohexane droplet showing excellent agreement with equivalent experiments. This validates the equation of state and promotes the use of numerical simulations as a valuable tool for understanding the complex acoustic interactions involved in these biomedical agents, ultimately facilitating their translation for clinical purposes.

Keywords: Perfluorohexane, equation of state, mesoscale gas-launcher, shock-induced droplet vaporization

## I. INTRODUCTION

Perfluorocarbons have recently gained traction as building blocks for acoustically-responsive agents in various biomedical applications [1]. Perfluorohexane (PFH,  $C_6F_{14}$ ), a heavier fluorocarbon, has long been investigated for its potential oxygen-carrying capacity [2] and as phase-change agents in the form of sub-micron droplets, which upon ultrasound activation are converted into microbubbles [3]. This process is typically called acoustic droplet vaporization (ADV) [4] and is leveraged in several theranostic applications, such as contrast-enhanced imaging, sonodynamic therapy, and targeted drug delivery [5–8]. Compared to the more established microbubbles, nanodroplets present higher circulation times *in vivo* enabling theranostic processes to be implemented for a longer duration [9]. Furthermore, their small size allows them to extravasate into the vascular space due to the Enhanced Permeability and Retention (EPR) effect and to interact directly with cancers and tumor cells, provided that EPR occurs during treatment [10]. However, ADV of droplets based on heavier perfluorocarbons requires high negative pressures for activation, which makes the process susceptible to off-target cavitation bioeffects and, therefore, unsafe for clinical use [1].

The mechanism of ADV initiation has been attributed to the acoustic impedance mismatch between perfluorocarbons and their surrounding medium (water and blood for example) leading to the focusing of the acoustic wave within the droplet [11, 12]. Recently, Fiorini *et al.* [12] have further shown that focusing of the compression phase of the incoming acoustic wave can generate negative pressures in the droplet bulk. This suggests that waves with high positive pressures and minimal tensile excitation such as therapeutic shock waves could be employed as acoustic sources to initiate phase change of droplets. Provided that they propagate in the human body with minimal interference and reflections, such shock waves can reduce undesirable bioeffects. High-amplitude shock waves, with peak pressures up to 100 MPa, have been clinically approved for therapeutic applications such as lithotripsy to treat kidney stones [13], while shock waves with peak pressures closer to 10 MPa are being explored for other delicate purposes such as stem cell and neuron activation [14, 15], microcirculation stimulation [16] and targeted drug delivery using nanobubbles [17, 18]. Although there has been preclinical research promoting shock wave interactions with nano- and microbubbles, further developments are hindered by their interactions being difficult to analyze due to their small spatiotemporal scales. This becomes even more complex in shock-induced droplet vaporization, as the physical mechanisms that trigger shock-droplet interactions are not yet fully understood. This lack of understanding still poses challenges for clinical translation.

Hydrodynamic, multiphase numerical simulations are a powerful tool that can contribute to building a better understanding of shock-droplet interaction and therefore, optimize the acoustic driving necessary to induce phase change within the drop. However, the modeling requires thermodynamically valid constitutive relations for the material

---

\* aanunay@ethz.ch

(PFH), *i.e.*, an equation of state (EOS) for closure, which are difficult to calibrate [19]. Existing thermodynamic equations of state for PFH are highly uncertain or have limited validity due to the scarcity of experimental data. Gao *et al.* [20] have reported Helmholtz energy equations of state for PFH that are valid for a large range of pressures and temperatures. However, to ensure the numerical stability of simulations utilizing high-pressure shock waves, leading to pressures larger than standard critical pressures of the material (2.045 MPa for PFH [20]), a more accurate and well-calibrated EOS tailored specifically for such phenomena needs to be obtained [21].

Shock compression-based experiments, which rely on inducing planar shock fronts in media to derive their EOS, are a well-established method, yet considerably more challenging for liquids than solids [22–25]. The Rankine-Hugoniot jump relations between the fluid state before and after the passage of a shock wave are used to establish a kinematic EOS as a base to obtain the desired EOS for numerical simulations [26, 27]. The Rankine-Hugoniot equation of state defines thermodynamic state variables as follows:

$$\begin{aligned} P - P_0 &= \rho_0(u_s - u_0)(u_p - u_0) \\ v &= v_0 \left[ 1 - \frac{u_p - u_0}{u_s - u_0} \right] \\ e - e_0 &= \frac{1}{2}(P + P_0)(v_0 - v), \end{aligned} \tag{1}$$

where  $P$  is the pressure,  $v$  is the specific volume,  $e$  is the internal energy,  $\rho$  is the material density,  $u_s$  is the shock wave velocity, and  $u_p$  is the particle velocity in the material behind the shock front. The subscript 0 in Eq. (1) refers to the initial state of the material. The EOS employed in numerical simulations governed by the Euler equations must be convex and hyperbolic in order to prevent the sound speed from becoming negative in unstable flows and for the simulation to be scientifically accurate [19, 28]. Such an EOS must therefore be developed from experimental data. Multi-objective optimization algorithms have recently been used to obtain EOS fits that can capture phase transitions and critical phenomena [29–31]. The method has proven adequate to accurately represent material properties.

In this work, we perform planar impact experiments using a mesoscale gas-launcher to first determine the  $u_s - u_p$  relation for PFH from which we utilize a multi-objective optimization program to derive the Noble-Abel Stiffened-Gas (NASG) EOS [32], which is suitable for hydrodynamic simulations. We validate the generated EOS by performing numerical simulations corresponding to the impact experiments as well as a PFH droplet interacting with a laser-induced shock wave, and compare the propagation of the shock front in the simulations with the experiments. This work establishes the framework to determine other EOS and thermodynamic properties for PFH and opens up prominent avenues for simulation-based study of reagents and nanodroplets using PFH.

## II. MATERIALS AND METHODS

### A. Experimental setup

#### 1. Impact experiments

The sample container and the sabot for the launcher represented in Fig. 1 are machined from polymethylmethacrylate (PMMA) and polycarbonate (PC), in accordance with previous experimental work [33]. The container consists of a cylindrical PMMA tube with an outer diameter of 20 mm and thickness of 2 mm. The tube is glued to a 1.7 mm thick driver plate, which presents a 1.3 mm long, 16 mm thick extrusion to increase the contact surface between the tube and the plate. The end cap is 3D-printed with UV-curable resin, has a trapezoidal section, and is also glued to the cylinder. The container is filled with PFH (Fluoromed,  $\rho_{\text{PFH}} = 1680.1 \text{ kg m}^{-3}$ ) using a through hole in the end cap, which is sealed using epoxy.

The sabot is machined in a dog-bone shape from PC and has a maximum diameter of 25 mm. Two O-rings (NBR O-ring 18×2.5 mm) are wrung around both ends of the sabot to hold it in place under vacuum. A PMMA flyer, attached to a copper plate and an additional PMMA piece to increase the sabot’s mass and lower its impact speed, is glued to the top of the sabot. The PMMA flyer is chosen to match the impedance of the impacting section to that of the container, simplifying the calculation of the particle velocities during post-processing.

The experiments are carried out using a mesoscale gas-launcher used in previous studies at the European Synchrotron Radiation Facility’s ID19 beamline [34]. A schematic showing the single-stage mode of the launcher, powerful enough to achieve the desired impact speeds of the present study, is depicted in Fig. 1. The sabot is loaded into the breech consisting of a reservoir of high-pressure helium gas and maintained under vacuum at time  $t_1$ . Adjusting the pressure of the helium gas allows for tuning the impact velocities of the sabot. The sample is loaded in the target chamber, also maintained under vacuum, and the base of the driver plate is aligned perpendicular to the sabot’s

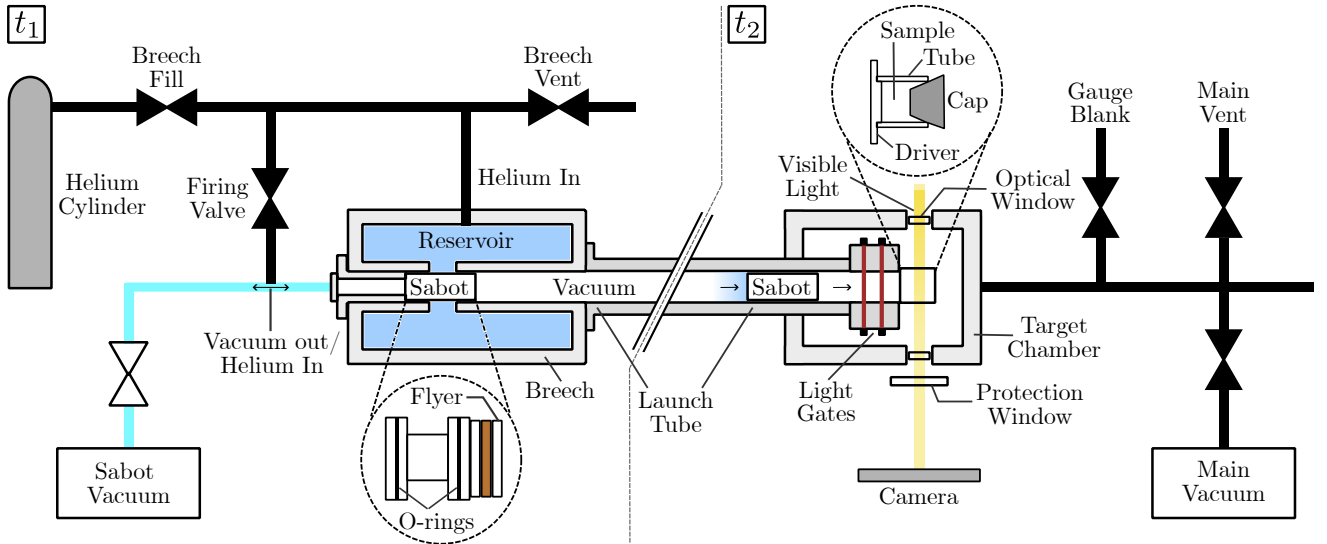


FIG. 1. Schematic of the experimental setup: At time,  $t_1$ , the sabot is located in the breach and held by vacuum. Upon filling the breach with Helium and firing (at time,  $t_2$ ), the sabot is shot forward with velocity  $u_f$  and impacts the container, which is located inside the target chamber, also maintained under vacuum. The light gates are separated by a known distance and enable precise calculation of the impact speed as the sabot passes through them.

propagation path to ensure planar impacts. The sample is simultaneously aligned perpendicular to the optical path, with high-speed shadowgraphy (Shimadzu HPV-X2 with LAOWA  $2.1\times$  zoom-lens, 2 – 5 million fps,  $0.4\text{--}0.5\times$  magnification) performed to visualize the shock wave propagation in PMMA and PFH. Optical windows are machined out of transparent PMMA sheets (2 mm thick), and a sturdier PMMA protection window (4 mm thick) is used to prevent any exploded material from damaging the high-speed camera setup. At time  $t_2$ , the sabot is launched down the 25 mm bore barrel connecting the breach to the target chamber. Along its path, the sabot cuts through two light gates separated by a known distance ( $d = 12.1$  cm). This system is based on two laser diodes connected to two photodetectors (Thorlabs, PDA10A2) having their read-out signal recorded on an oscilloscope (LeCroy Waverunner 9020). The recorded timings provide an accurate measurement of the impact velocity and trigger the high-speed camera, thereby completing one measurement.

## 2. Shock-droplet interaction setup

The experimental setup employed for visualizing the shock-droplet interaction is depicted in Fig. 2. PFH droplets with radius  $R = 600 - 1000$   $\mu\text{m}$  are placed on a 2% w/v agarose gel plate and immersed in a water tank. Shock waves are generated, approximately 5 mm away from the droplet location, by optical breakdown of water using a frequency-doubled, pulsed Nd:YAG laser (Lumibird Quantel Q-smart, 6 ns, 532 nm). The beam is first expanded using a  $10\times$  beam expander (52-71-10X-532/1064, Special Optics) and then focused by a  $90^\circ$  parabolic mirror (Edmund Optics,  $f = 50$  mm) to generate a spherically propagating shock wave. The shock profile is measured  $d = 4$  cm away from the focus using a  $75$   $\mu\text{m}$  needle hydrophone (Precision Acoustics, NH0075) and then extrapolated to obtain the peak pressure at the droplet location (see Bokman *et al.* [35] for full details). The shock wave is spherically propagating and shows an exponentially decaying profile as depicted in Fig. 2(c). The Friedlander equation is used to approximate an idealized shock profile as  $P_a(t) = P_{\text{max}}(1 - t/t_1) \exp(-bt/t_1)$ , where  $P_{\text{max}}$  is the peak pressure,  $t_1$  is the total duration of the shock wave, and  $b$  is a fitting parameter obtained from the hydrophone measurements. Such a curve is superimposed on top of the experimental measurements with  $P_{\text{max}} = 21.7$  MPa,  $t_1 = 428$  ns, and  $b = 10$  in Fig. 2(c). High-speed shadowgraphy is performed to visualize the shock wave within the droplet. A pulsed red laser (645 nm) illumination system (Cavitar, Cavilux Smart UHS) with a pulse duration time of  $t_{\text{ex}} = 10$  ns is used to obtain images of the shock front propagation. The video is recorded at 10 million fps by a high-speed camera (Shimadzu HPV-X2). The laser illumination and the high-speed camera are synchronized and both are triggered by the Nd:YAG laser through a delay generator (Stanford Research Systems, DG645).

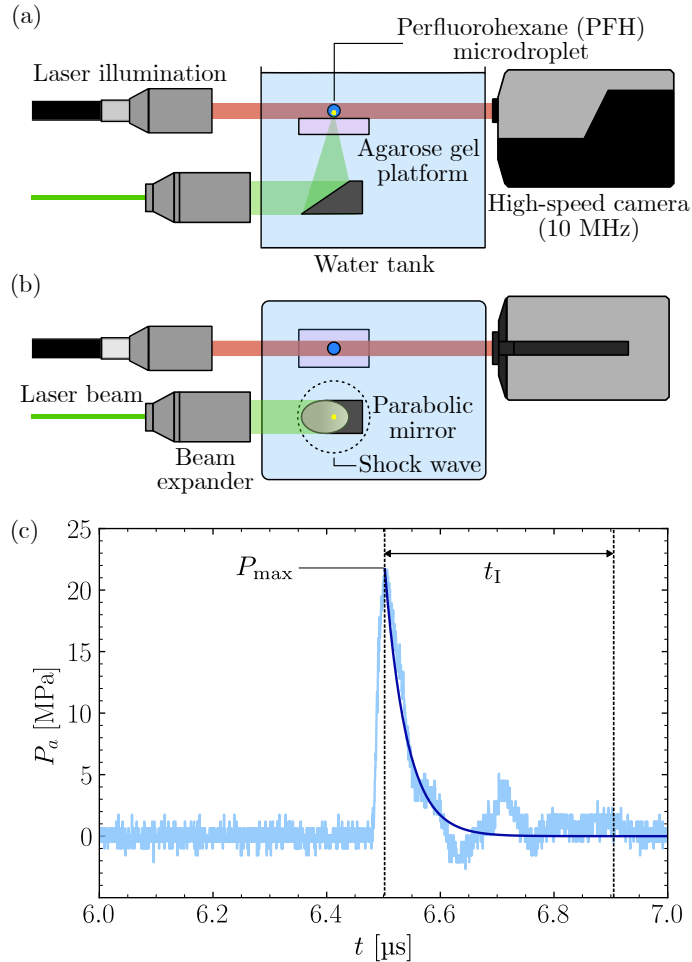


FIG. 2. Experimental setup to capture the shock front propagation in a PFH droplet. (a) Side view: A droplet is positioned on a gel platform and imaged with a frame rate of 10 million fps. (b) Top view: The shock wave is generated by laser-induced breakdown at the focal point of a parabolic mirror. The generated spark is positioned at the same height as the droplet and arranged so that the propagating shock front hits the droplet at a position perpendicular to the illumination path. (c) Experimental pressure profile of the shock wave at the droplet's location (light blue line) superimposed by the idealized waveform (dark blue line) computed using the Friedlander equation with  $P_{\max} = 21.7$  MPa,  $t_I = 428$  ns, and  $b = 10$ .

## B. Numerical simulations

Hydrodynamic simulations are performed using ECOGEN, a thermodynamically well-posed, multiphase, compressible, diffuse interface method [36]. ECOGEN has been validated for several configurations including interactions of bubbles [37] and droplets [38, 39] with shock waves. The governing equations are the modified Euler equations with relaxation procedures as described in Kapila *et al.* [40] and Richard Saurel *et al.* [41] and are given as:

$$\begin{aligned}
 \frac{\partial \alpha_j}{\partial t} + \mathbf{u} \cdot \nabla \alpha_j &= \delta p_j \\
 \frac{\partial \alpha_j \rho_j}{\partial t} + \nabla \cdot (\alpha_j \rho_j \mathbf{u}) &= 0 \\
 \frac{\partial \rho \mathbf{u}}{\partial t} + \nabla \cdot (\rho \mathbf{u} \otimes \mathbf{u} + P \mathbf{I}) &= 0 \\
 \frac{\partial \rho E}{\partial t} + \nabla \cdot [(\rho E + P) \mathbf{u}] &= 0
 \end{aligned} \tag{2}$$

where the subscript  $j = 1, 2, \dots, N$  corresponds to the  $N$  phases in the simulation. The volume fraction and density of each phase are denoted by  $\alpha_j$  and  $\rho_j$  respectively, and  $\delta p_j$  is the pressure-relaxation term for each phase. The

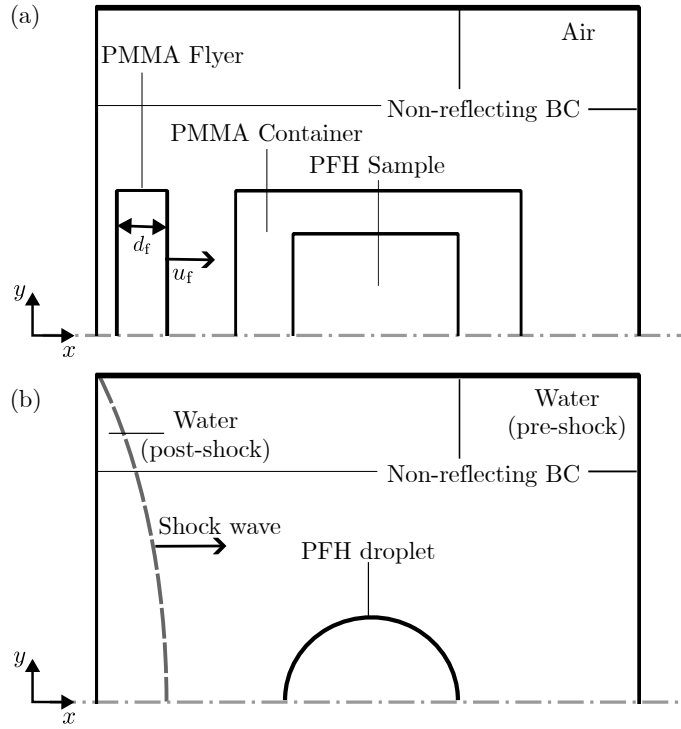


FIG. 3. Schematic depicting the initial numerical setup (a) Impact experiment: A PMMA flyer of thickness,  $d_f$  with impact velocity  $u_f$  is launched towards a PMMA container loaded with liquid PFH. (b) Shock-droplet interaction experiment: A spherically propagating shock wave, propagating towards the right, is initiated on the left side of the domain and interacts with a circular PFH droplet. All simulations are 2D axisymmetric.

mixture velocity and pressure are represented by  $\mathbf{u}$  and  $P$ . The mixture density is defined as,  $\rho = \sum_j \alpha_j \rho_j$ . The total energy is denoted by  $E$ , and is defined as  $E = e + \frac{1}{2} \|\mathbf{u}\|^2$ , where  $e = \sum_j \alpha_j \rho_j e_j$  is the mixture internal energy. Constitutive EOS for the different materials are employed to relate the speed of sound to the pressure in the fluid. The ideal gas law is used as an EOS for air

$$P_{\text{air}} = \rho_{\text{air}} (\kappa_{\text{air}} - 1) (e_{\text{air}} - e_{\text{air,ref}}) \quad (3)$$

where  $\kappa_{\text{air}} = 1.4$  and  $e_{\text{air,ref}} = 0 \text{ J kg}^{-1}$  are model parameters [42] and  $\rho_{\text{air}} = 1.2 \text{ kg m}^{-3}$  is the density of air. Water is modeled using the stiffened gas EOS

$$P_w = \rho_w (\kappa_w - 1) (e_w - e_{w,\text{ref}}) - \kappa_w \Pi_\infty \quad (4)$$

where  $\Pi_\infty$  is another model parameter, with  $\kappa_w = 2.955$ ,  $e_{w,\text{ref}} = 0 \text{ J kg}^{-1}$ ,  $\Pi_\infty = 7.22 \times 10^8 \text{ Pa}$  and  $\rho_w = 996 \text{ kg m}^{-3}$  is the density of water. Both of these EOSes are well-validated for ECOGEN through several case studies [36–39]. For PMMA and PFH, the Noble-Abel Stiffened-Gas (NASG) EOS is employed [32].

$$e(P, v) = \frac{P + \gamma P_\infty}{\gamma - 1} (v - b) + q \quad (5)$$

$$v(P, T) = \frac{(\gamma - 1) C_v T}{P + P_\infty} + b \quad (6)$$

$$h(P, T) = C_p T + b P + q \quad (7)$$

where  $e, P, v, T, h$  are the internal energy, pressure, specific volume, temperature, and enthalpy of the material respectively. The other variables are the specific heat at constant pressure and volume,  $C_p, C_v$ , and their ratio  $\gamma$ . The specific volume parameter,  $b$  accounts for the repulsive effects between the molecules of the material, while  $P_\infty$  is a stiffness parameter to indicate that materials can withstand a degree of tension without changing phase [19]. The NASG EOS also requires the definition of a reference entropy,  $q'$ , which we set equal to zero following the convention for liquids [32]. From Eq. (5) and the thermodynamic definition of the speed of sound in the material, we get

$$c^2 = \left( \frac{\partial p}{\partial \rho} \right)_s = \frac{\gamma (P + P_\infty)}{\rho (1 - b \rho)} \quad (8)$$

All the above EOSes are fitted from  $u_s - u_p$  relations, either available from literature (air, water [32] and PMMA [43]) or from the experimental data collected within the present work (PFH). The system of equations described above is solved using an implicit time-integration scheme, which is a standard procedure for such equations. Further details about the numerical scheme employed are fully described elsewhere [36, 39].

In order to validate the EOS obtained herein, two-dimensional, axisymmetric numerical simulations of the impact experiments are performed. A schematic depicting the domain is provided in Fig. 3(a). A PMMA projectile simulating the flyer with thickness 4 mm and the same initial velocity as measured in the experiments is launched into a cylindrical PMMA tube (ID = 16 mm, OD = 20 mm,  $\rho_{\text{PMMA}} = 1185 \text{ kg m}^{-3}$ ,  $P_1 = 101.3 \text{ kPa}$ ) containing liquid PFH ( $\rho_{\text{PFH}} = 1680.1 \text{ kg m}^{-3}$ ,  $P_{0,\text{PFH}} = 101.3 \text{ kPa}$ ). The external medium is simulated as air at ambient conditions ( $\rho_{\text{air}} = 1.2 \text{ kg m}^{-3}$ ,  $P_3 = 101.3 \text{ kPa}$ ).

We further simulate the shock-droplet interaction to validate the employed EOS with a different case as compared to the experiments used to determine the EOS itself. This provides the pressure field within the droplet as the shock front propagates in it. The PFH droplet ( $\rho_{\text{PFH}} = 1680.1 \text{ kg m}^{-3}$ ,  $P_{0,\text{PFH}} = 101.3 \text{ kPa}$ ) is modeled as a circular discontinuity placed in an infinite medium of water ( $\rho_w = 996 \text{ kg m}^{-3}$ ,  $P_{0,w} = 101.3 \text{ kPa}$ ) in a two-dimensional, axisymmetric setting as depicted in Fig. 3(b). The idealized shock wave pressure profiles (see Fig. 2(c)) are initiated as spherically propagating discontinuities in water. Reference properties for both simulation cases were defined at a temperature of  $T = 25 \text{ }^\circ\text{C}$ .

By definition, shadowgraphy is the integral of the second derivative of the density along the optical path [44]. Computing this numerically would require information about the Gladstone-Dale constant for PFH, which is not available [45]. Therefore, we resort to numerical Schlieren to capture the propagation of the shock front in different media, since the shock wave is the source of the largest density gradient within our field of view. This is evaluated using the equation given below

$$S_n = 1 - \exp\left(\frac{\|\nabla\rho\|}{\|\nabla\rho\|_{\text{max}}}\right) \quad (9)$$

where  $\|\nabla\rho\|$  is the magnitude of the density gradient and  $S_n$  is the numerical Schlieren field, which is then compared to the locations of experimentally visualized shock fronts.

### C. Estimation of particle velocity and kinematic EOS for PFH

The well-known shock-impedance matching technique [19, 25] is used to estimate the particle velocity in PFH and is briefly described below. Here, the container (with quantities denoted by subscript 'c') and flyer (with quantities denoted by subscript 'f') are designed out of PMMA ( $\rho_{\text{PMMA}} = 1185 \text{ kg m}^{-3}$ ), and the contained liquid (with quantities denoted by subscript 'l') is PFH ( $\rho_{\text{PFH}} = 1680.1 \text{ kg m}^{-3}$  at  $25 \text{ }^\circ\text{C}$ ). Since the objects are initially at rest and maintained under vacuum,  $u_0$  and  $P_0$  are negligible in Eq. (1) and are taken as zero to simplify the calculation. After impact, all objects are in a post-shock state, with a given particle velocity and pressure as indicated in Fig. 4(a). To estimate the post-shock states of the different objects, first, the Hugoniot pressure of the container is evaluated using Eq. (1) as a function of the particle velocity of the container and its expected shock wave velocity:

$$P_c = \rho_{\text{PMMA}} u_{p,c} u_{s,c} \quad (10)$$

In general, the shock velocity can be approximated as a polynomial function of the particle velocity. For PMMA, the expression takes the form [43]

$$u_s = 6.486u_p^3 - 7.823u_p^2 + 3.549u_p + 2.703, \quad (11)$$

for  $u_p \leq 0.4 \text{ km s}^{-1}$

where  $u_s$  is the expected shock velocity for a given particle velocity,  $u_p$ , in PMMA. Then, the expected shock velocity in the container,  $u_{s,c}$ , can be evaluated by substituting  $u_p = u_{p,c}$  in Eq. (11). At a contact discontinuity, the pressure and particle velocity are considered to be continuous for a planar impact [46]. Therefore, the pressure in the flyer, which has an initial particle velocity of  $u_f$  (equivalent to its launch speed), decreases such that its value is equivalent to the pressure in the container. This implies that the particle velocity of the flyer reduces from  $u_f$  to  $u_{p,c}$ , and therefore, the pressure in the flyer can be calculated using Eq. (1) as

$$P_f = \rho_{\text{PMMA}} (u_f - u_{p,c}) u_{s,f}, \quad (12)$$

where  $u_{s,f} = f(u_f - u_{p,c})$  is again estimated using Eq. (11). The intersection of the container [Eq.(10)] and flyer Hugoniot [Eq. (12)] determines the particle velocity in the container,  $u_{p,c}$ , as depicted in Fig. 4(b). It can be shown

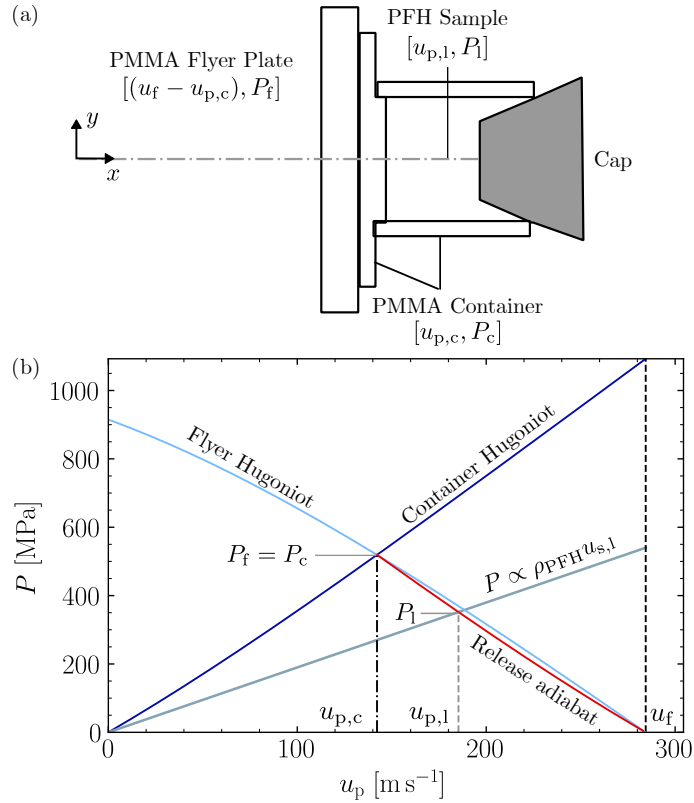


FIG. 4. (a) Schematic depicting the post-shock particle velocity - pressure pairs,  $(u_p, P)$ , expected in the flyer, the container and the PFH sample. The particle velocity in PFH is determined by the intersection of the release adiabat,  $P_r$ , with a straight line of slope  $\rho_{\text{PFH}} u_{s,l}$ , where  $u_{s,l}$  is the shock velocity in the liquid. (b) Graphical depiction of the shock impedance matching technique to determine the expected particle velocity in PFH within the PMMA container for the mesoscale gas launcher experiments.

that  $u_{p,c} = u_f/2$ . The release of the container pressure into the liquid stored in it is assumed to follow an isentropic process. Since PFH has a lower impedance than PMMA, to ensure the continuity of pressure between the two media, this adiabatic release increases the pressure within the liquid leading to a higher particle velocity than at the container wall. The particle velocity for such a process can be evaluated from the Riemann integral between the limits of  $P_c$  to the expected pressure in the liquid,  $P_l$  [19]:

$$u_r = u_{p,c} + \int_{P_c}^{P_l} \frac{dP}{\rho c}, \quad (13)$$

where  $u_r$  is the particle velocity and  $c$  is the sound speed associated with a given pressure along the release adiabat. Using Eq. (1), the integral in Eq. (13) can be transformed from the  $P - u_p$  plane into the  $u_s - u_p$  plane to evaluate  $u_r$  as

$$u_r = u_{p,c} + \int_{u_{p,c}}^{u_{p,l}} \sqrt{1 - \left( \frac{u_{s,c}}{u_{p,c}} \frac{du_{s,c}}{du_{p,c}} \right)^2} du_p, \quad (14)$$

where  $u_{p,c}$  and  $u_{p,l}$  again represent the particle velocities expected in the container and the PFH liquid. Here, the derivative  $du_{s,c}/du_{p,c}$  is calculated from Eq. (11) (since the container is machined from PMMA). Then, the pressure along the release adiabat is given by

$$P_r = \rho_{\text{PMMA}} u_r u_{s,r}, \quad (15)$$

where  $u_{s,r} = f(u_r)$  is yet again calculated from Eq. (11). Different values of  $(u_r, P_r)$  along the isentrope are evaluated by setting different expected values of  $u_{p,l}$  and calculating the integral given in Eq. (14). The particle velocity in the liquid PFH,  $u_{p,l}$ , is then estimated by the intersection of the release adiabat with a straight line passing through the origin and having a slope of  $\rho_{\text{PFH}} u_{s,l}$ , as shown in Fig. 4(b).

### D. Multi-objective optimization for EOS parameter determination

The estimated kinematic EOS is used to generate the necessary parameters ( $b$ ,  $\gamma$ ,  $C_p$ ,  $C_v$ ,  $P_\infty$ ) for a complete NASG EOS as defined in Sec. II B. This is done by reformulating Eqs. (5) and (6) along with Eq. (1) into cost functions for a multi-objective, least-squares optimization problem. The formulation is subjected to equality constraints in the form of Eq. (8), ensuring that the fitted parameters reproduce the correct speed of sound for the material at reference properties extracted from literature [43, 47]. The complete system is expressed as follows:

$$\begin{aligned}
 \min f_1 &= \sum [(e - e_0)_{\text{exp}} - (e - e_0)_{\text{NASG}}]^2 \\
 \min f_2 &= \sum [(v - v_0)_{\text{exp}} - (v - v_0)_{\text{NASG}}]^2 \\
 \text{s.t. } P_0 + P_\infty &= \left[ \left( 1 - \frac{C_p - C_v}{C_p} \right) \rho_0 c_0^2 (1 - b\rho_0) \right] \\
 C_p/C_v - \gamma &= 0.
 \end{aligned} \tag{16}$$

The multi-objective optimization problem is solved using the PyMOO module in Python [48]. A Non-sorted Genetic Algorithm (NSGA-II) is used to find the parameters for the NASG EOS [49]. To reach the Pareto optimal solution as efficiently as possible, a simulated binary crossover (SBX) with polynomial mutation is applied to improve the quality of the offspring produced at every generation [50]. The crossover and mutation parameters were set to balance the creation of feasible offspring while exploring the objective space efficiently, without excessive computational cost. NSGA-II has been tested on several bi-objective problems and is shown to be highly computationally efficient due to its elitist approach, and therefore, chosen as the most suitable algorithm to solve Eq. (16) [49, 50].

To obtain a suitable termination criterion and to ensure the quality of the obtained optimization results, it is necessary to monitor the performance of the run. Typically, this involves evaluating certain performance metrics with respect to a reference set (usually the known Pareto front) generation-by-generation. However, this requires *a priori* knowledge of the Pareto optimal solution, which is not possible for our optimization problem. Therefore, the simulation convergence is monitored using running metrics such as the normalized ideal and nadir points, and the normalized, redefined Inverted Generational Distance (IGD) between successive generations [51]. As a suitable termination condition, we monitor the movement of the objective functions and the above-mentioned parameters per consecutive generations and terminate the optimization when their movement lies below a set tolerance for a given number of successive generations. Termination and convergence criteria are discussed further in Sec. III and Appendix A.

## III. RESULTS

As the sabot is launched and impacts the sample container in the mesoscale gas-launcher experiments, forward- and backward-propagating planar shock waves are produced at the contact discontinuity. Owing to the higher speed of sound in PMMA as compared to PFH, the forward-propagating wave travels faster in the PMMA container than in the PFH sample. The backward-propagating wave is further reflected from the attached copper mass on the sabot, while the forward-propagating wave is deflected at the edges of the container, propagating through the epoxy coating used to hold the container together. The combined effects of the waves promote complex acoustic interactions within the container leading to its cracking. The cracks expose the sample to vacuum, thereby causing a sudden pressure drop in the liquid that results in cavitation. Consequently, only the initial forward-propagating shock is employed to estimate the kinematic EOS of both materials and the other complex waves are neglected. Thirteen shots with impact velocities between 104–280  $\text{m s}^{-1}$  are used to estimate the necessary quantities.

### A. Shock-wave propagation in PMMA

The velocity of the initial shock wave traveling in the PMMA container is measured from the experimental shadowgraph images for different impact velocities (see video in Supplemental Material and Fig. 7 for sample shadowgraphs) and plotted in Fig. 5. Since our experimental particle velocities are low, the dependency between the shock wave and particle velocity in PMMA is non-linear [23, 43]. As depicted in Fig. 5, our measured shock wave velocities correspond quite well to the cubic polynomial relation connecting the shock and particle velocity in PMMA for  $u_p < 0.4 \text{ km s}^{-1}$  obtained from Jordan *et al.* [43] and given by Eq. (11). The shaded gray area shows the 2% uncertainty that Jordan *et al.* [43] expect from their results, while the error bars for the experimental values arise from the uncertainty

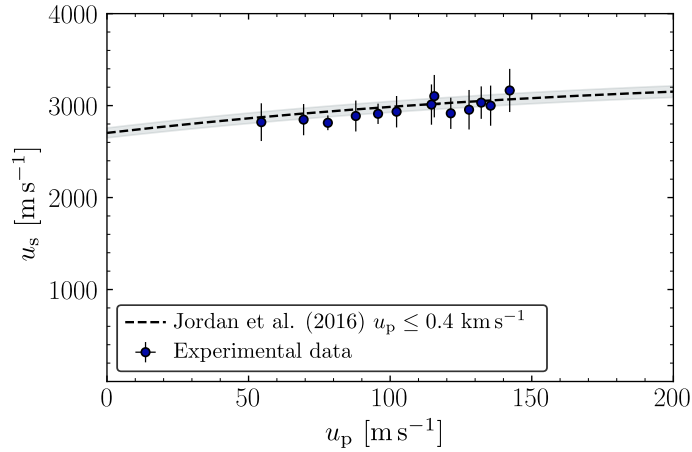


FIG. 5. Experimentally determined shock wave velocity in the PMMA container compared to the EOS obtained from Jordan *et al.* [43]. Error bars represent the experimental uncertainty associated with the shock velocity measurements. The gray shaded area represents the error expected by Jordan *et al.* [43] in their results.

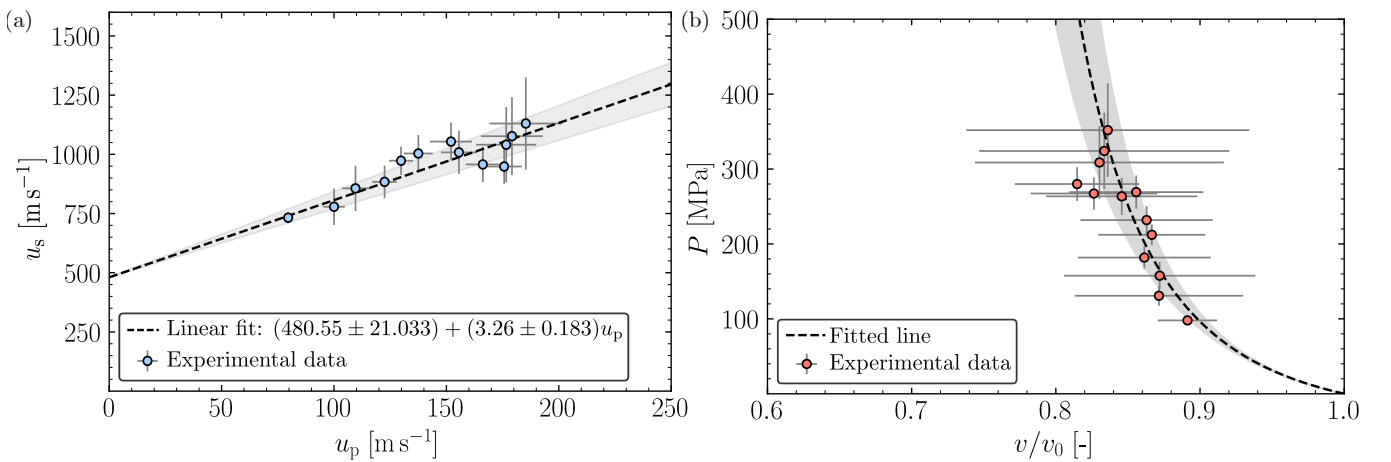


FIG. 6. (a) Kinematic equation of state depicted in terms of the shock velocity,  $u_s$ , as a function of the particle velocity,  $u_p$ , for PFH. The dashed line plots the linear fit obtained using orthogonal distance regression, with the shaded area indicating the uncertainty associated with it. This uncertainty arises as a direct consequence of considering the experimental errors in both  $u_s$  and  $u_p$  while performing the fitting. (b) The Hugoniot for PFH is plotted in terms of the pressure versus relative volume, with the dashed line showing the expected theoretical curve obtained by evaluating the shock velocity from the linear fit depicted in (a). The gray shaded area again depicts the associated uncertainty similar to (a).

associated with the distance travelled by the shock waves between two frames. Details for the calculation of our experimental errors are provided in Appendix B.

Fig. 5 validates Eq. (11) as the kinematic EOS of PMMA for our experiments to determine the necessary thermodynamic state variables from the Rankine-Hugoniot set of equations [Eq. (1)]. This is then transposed to the experimentally defined state variables of the minimization functions as described in Eq. (16) to determine the NASG EOS of PMMA for our numerical simulations.

## B. Kinematic EOS of PFH

Similar to the shock wave propagation in PMMA, the shock velocity in PFH ( $u_{s,\text{PFH}}$ ) is estimated from the high-speed images obtained experimentally (see Fig. 7 for sample shadowgraphs). This process is repeated for all the different impact velocities recorded experimentally. Fig. 6(a) plots the dependence of the shock velocity on the particle velocity in PFH. The error bars represent the maximum uncertainty associated with the shock velocity and the particle velocity, estimated using a Monte-Carlo error propagation technique as detailed in Appendix B. The

shock velocity in PFH varies approximately linearly with the particle velocity, although this becomes unclear for higher particle velocities, where the experimental errors become significant.

Orthogonal distance regression [52] is used to obtain a linear fit of the form  $u_s = c_0 + au_p$ , with  $c_0$  depicting the estimated base speed of sound. This method was preferred to account for the experimental errors in both  $u_{p,\text{PFH}}$  and  $u_{s,\text{PFH}}$ , and to avoid biasing the fitting process towards the highly uncertain values at larger particle velocities. Therefore, the kinematic EOS for PFH can be given as

$$u_{s,\text{PFH}} = (480.55 \pm 21.033) + (3.26 \pm 0.183)u_p. \quad (17)$$

We decided not to constrain the base speed of sound for the fit, although constraining it to reference speeds of sound observed between the temperatures of  $T = 20 - 25$  °C did not significantly alter the slope of the line. The associated experimental errors imply that the obtained kinematic EOS is more accurate for lower particle velocities, and therefore at lower Mach values.

Fig. 6(b) depicts the  $P - v$  Hugoniot up to the pressure of 500 MPa, with the dashed line indicating the expected Hugoniot evaluated from combining Eq. (1) with Eq. (17). Although the maximum error in the relative volume reaches 12%, the overall fit remains satisfactory. The thermodynamic state variables of PFH can now be evaluated using Eq. (1) in conjunction with Eq. (17) transposed to Eq. (16), and used to fit the NASG EOS for PFH.

### C. Fitting parameters for NASG EOS

Once the  $u_s - u_p$  relations for both materials are determined, we can formulate our optimization cost functions,  $f_1$  and  $f_2$  defined in Eq. (16). This is done by selecting the appropriate reference state of the materials in order to define the constraints of the problem. First, we set the reference temperature at which the respective experiments are performed as  $T = 25$  °C. Then, we determine the speed of sound, density, and an approximate range of specific heats for the materials [20, 53]. Selecting a slightly higher or lower reference temperature ( $\pm 2$  °C) did not alter the results, but some cases required the speed of sound to be adjusted at the corresponding temperature, as discussed later. Since multiple combinations of the equation parameters can be possible solutions for the NASG problem, we set the upper and lower bounds of our fitted parameters using the information available above. This constrains the optimization between known bounds and prevents the search algorithm from exploding. The specific heats ( $C_p$ ,  $C_v$ ) are given a small range in between the experimentally measured values obtained from literature [20, 53], while the other parameters ( $b$ ,  $\gamma$ ,  $P_\infty$ ) are given ranges similar to values expected for other materials [28, 32, 42].

The optimization is performed using the NSGA-II algorithm with the evolutionary operators selected so as to speed up the computation, as described previously in Sec. IID. A population size of 400 offspring per generation is employed with simulated binary crossover and polynomial mutation operators to enhance the diversity of the feasible children [49]. The convergence of the optimization program is monitored using the quantities described in Appendix A. The tolerance for convergence is set as  $\epsilon = 0.001 = 0.1\%$  and the simulation is terminated when the average tolerance of the last  $\chi = 100$  generations is less than  $\epsilon$  [51]. A further decrease in  $\epsilon$  or an increase in  $\chi$  did not significantly influence the results. The optimization is also allowed to run for longer durations ( $n_{\text{gen}} = 10000, 25000, 50000, 100000$ ) by ignoring the termination conditions set above to check if there is any significant movement in the objective or design space at later generations. This is found to be unimportant, implying that our set termination criteria is satisfactory.

Once the Pareto front has been obtained, suitable parameters for the EOS must be selected. We employ the in-built Augmented Scalarized Function (ASF) option in PyMOO [48]. ASF decomposes the multi-objective problem into single objectives and scalarizing functions are derived from a reference point in the objective space. These scalarizing functions are such that they have their minima located at Pareto points only, thereby allowing the selected point in the objective space to be a Pareto-optimal solution [54]. Equal weightage is provided to both objective functions and ASF is then applied to obtain the parameters. The selected parameters used to define our NASG equations for PMMA and PFH are listed in Table I, which are then used for the numerical simulations in ECOGEN.

TABLE I. Values of constants required to define the NASG EOS for PMMA and PFH.

Constant	PMMA	PFH
$\gamma$ [-]	1.466	1.276
$b$ [ $\text{m}^3 \text{kg}^{-1}$ ]	$7.58 \times 10^{-4}$	$1.033 \times 10^{-4}$
$C_v$ [ $\text{J kg}^{-1} \text{K}^{-1}$ ]	986.74	509.756
$C_p$ [ $\text{J kg}^{-1} \text{K}^{-1}$ ]	144.65	650.688
$P_\infty$ [Pa]	$5.927 \times 10^8$	$2.557 \times 10^8$
$q$ [ $\text{J kg}^{-1}$ ]	$-423.842 \times 10^3$	$-193.833 \times 10^3$

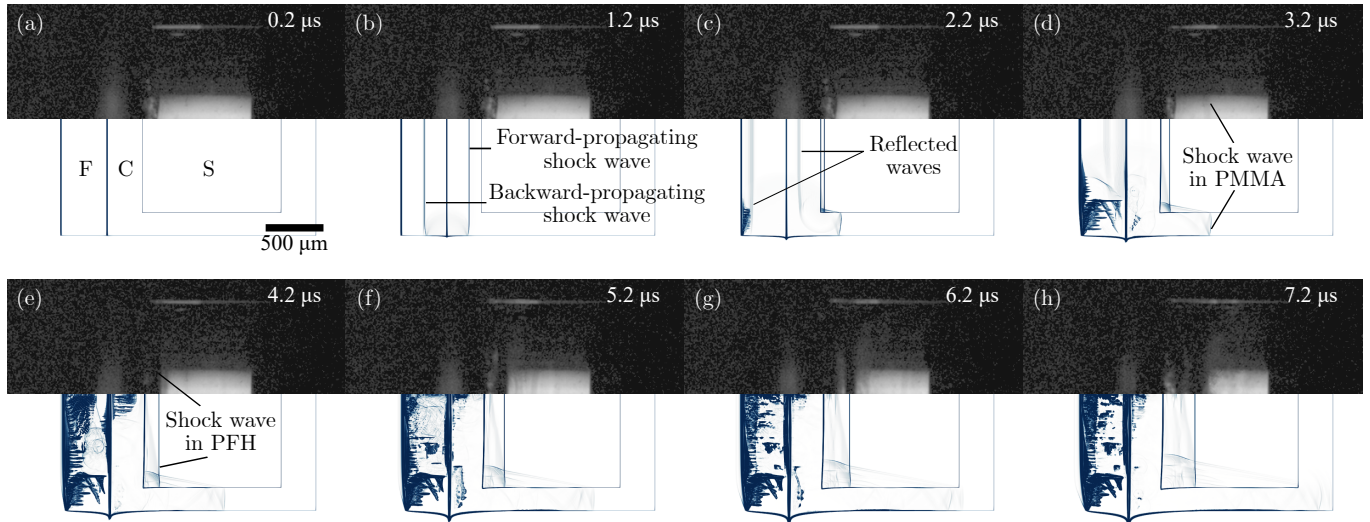


FIG. 7. Comparison of the experimental shadowgraphs (*top*) to the numerical Schlieren (*bottom*) for the test case with initial impact velocity of  $u_f = 109 \text{ m s}^{-1}$ . Here,  $t = 0$  indicates the instant when the impact occurs. (a) Moment shortly after impact. The PMMA flyer (F), PMMA container (C), and PFH sample (S) are labeled for reference. (b) Upon impact, forward- and backward-propagating shock waves are generated. (c) The interaction of these waves with the container wall and the walls of the flyer induces reflected waves, some of which are visible in the simulation. (d) The shock wave propagating in the PMMA container. (e) The shock wave propagating in PFH becomes clearly visible in the experiment. (f-g) Continued propagation of the waves and multiple spurious reflections due to complex acoustic interactions. Cavitation of the liquid, due to the reflected waves and the tensile tail of the shock wave, leads to a darkened image trailing the shock wave.

## D. Numerical validation

### 1. Impact experiments

As a first validation case, the impact experiment is simulated with a PMMA flyer launched at a given impact speed  $u_f$  into a PMMA container containing the PFH sample. Along with the aforementioned reference properties (see Sec. II B), the speed of sound for the different media are defined as follows:  $c_{0,\text{air}} = 343 \text{ m s}^{-1}$ ,  $c_{0,\text{PMMA}} = 2703 \text{ m s}^{-1}$  [43],  $c_{0,\text{PFH}} = 484.975 \text{ m s}^{-1}$ . The initial velocity of the container and the sample are set as  $u_0 = 0 \text{ m s}^{-1}$ . The epoxy resin used as an adhesive to secure the container, along with the attached copper mass of the sabot and the container's end cap, are omitted from our numerical setup. Including these elements increases the complexity and requires additional EOS for the materials (copper and resins), without significantly influencing the shock wave transmission and propagation into the PFH sample.

A qualitative comparison between the experiments and numerical simulations is depicted in Fig. 7 for an impact speed of  $u_f = 109 \text{ m s}^{-1}$ . The results discussed herein are equivalently valid for the other tested impact speeds ( $109\text{--}280 \text{ m s}^{-1}$ ). Snapshot (a) shows the moment shortly after impact, which occurs at time  $t = 0$ . The impact generates a forward-propagating shock wave in the PMMA container [labeled C in Fig. 7(a)] and a backward-propagating shock wave in the PMMA flyer [labeled F in Fig. 7(a)] as seen from the numerical Schlieren snapshot in Fig. 7(b). These waves are reflected at the back of the flyer and the container wall as shown in Fig. 7(c). These waves are not clearly visible in the experiments as their magnitude is expected to be lower than the still propagating forward shock wave, which is visualized in the shadowgraphs for the first time in Fig. 7(d), and whose location matches well with the numerical result. This validates our fitted NASG equation for PMMA obtained using Eqs. (1), (11), and (16). In the numerical Schlieren, the shock wave propagating in PFH is already visible from Fig. 7(c), while it is initially obscured by the shadow of the container and the epoxy holding it in the experimental shadowgraphs and only becomes visible in the shadowgraph at a later stage in Fig. 7(e). The correspondence between the experimental and numerical shock wave is reasonable, with the numerical shock wave being slightly slower. This correspondence is deemed acceptable considering the complexity of the problem, and the minor discrepancies could be attributed to the measured experimental errors and the fact that the EOS obtained for the numerical simulation is a statistical fit.

The numerical snapshots from Fig. 7(c-h) include large density gradients that continuously grow over time, at the corners of the flyer and the container. They arise due to the complex interaction of the reflected waves from the contact

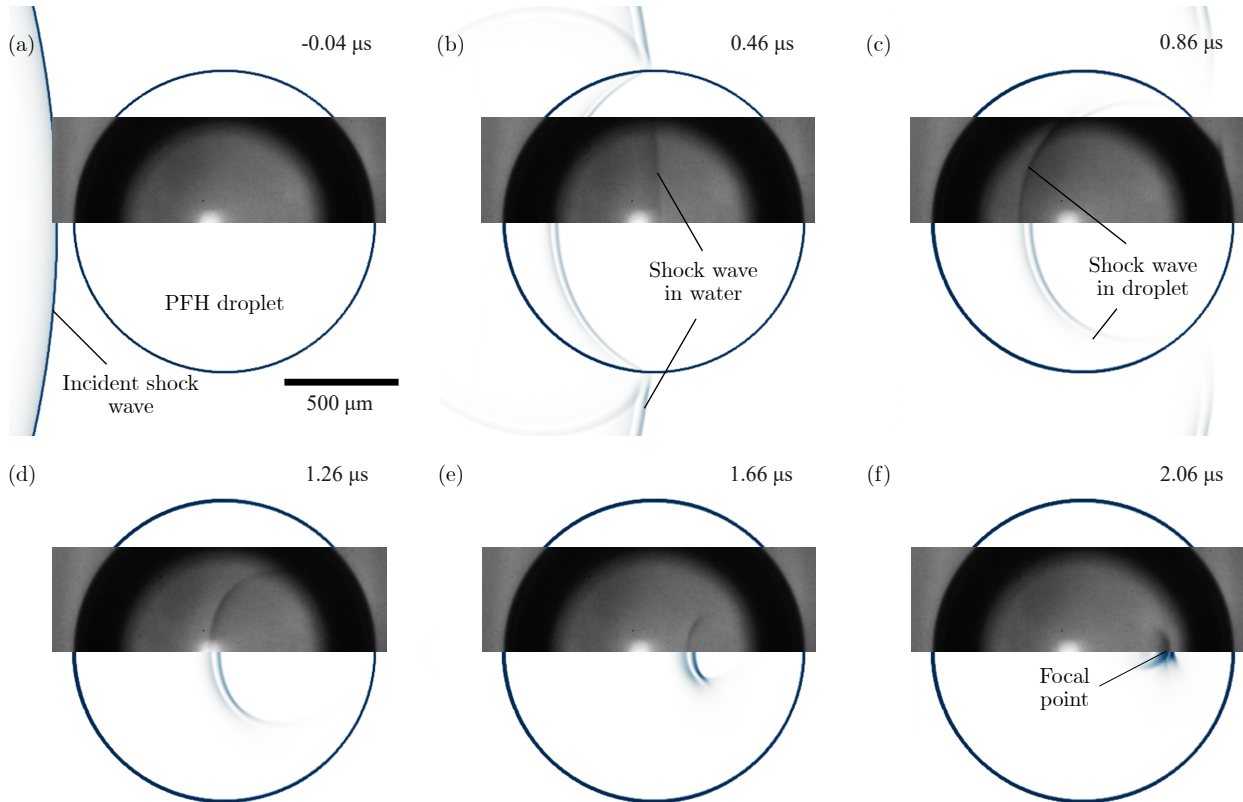


FIG. 8. Comparison of the experimental shadowgraphs (*top*) to the numerical Schlieren (*bottom*) for the test case with a laser-induced shock wave in water interacting with a PFH droplet of radius  $R = 662 \mu\text{m}$ . Here,  $t = 0$  indicates the instant the shock first interacts with the droplet. (a) A decaying, spherically propagating shock is initiated behind the PFH droplet. (b) The shock wave travels faster in water compared to the droplet and is visualized here. (c) The shock shape inside the droplet is clearly visible. The shock propagates further in the droplet (d–e) before focusing and amplifying the pressure at the focal point indicated in (f).

interfaces in the simulation and are deemed unphysical. Complex wave interactions did exist in the experiments and led to several other phenomena such as the cracking of the container, spallation, and the formation of cavitation bubbles within the PFH sample. Nonetheless, the number of frames available to reliably measure the shock wave speed is always sufficient. The numerical modeling of these phenomena is out of the scope of the study as they do not affect the determination of the EOS for PFH.

## 2. Shock-droplet interaction

We further validate our NASG EOS for PFH with another test case. In the shock-droplet interaction experiment, a laser-induced shock wave is generated in water and allowed to propagate into the PFH droplet. As mentioned previously in Sec. IIA 2, the waveform of the shock wave is measured experimentally using the hydrophone and is approximated using the Friedlander equation. The results below are given for a shock wave of peak pressure,  $P_{\text{max}} = 21.7 \text{ MPa}$ , with  $t_1 = 428 \text{ ns}$  and  $b = 10$ . Here, we define the reference speeds of sound for water and PFH as:  $c_{0,w} = 1481 \text{ m s}^{-1}$  [42],  $c_{0,\text{PFH}} = 484.975 \text{ m s}^{-1}$ .

Fig. 8 qualitatively compares the experimental shadowgraphs to the numerical Schlieren results. A spherically propagating shock wave (traveling left to right in the images) is initiated behind the droplet and reaches it at  $t = 0$ . The shock wave, having a faster speed in water than in PFH, is visible in the experiment in Fig. 8(b). The shock wave in PFH is obscured by the dark edge of the droplet (caused by the refraction from the curved interface) in Fig. 8(b), but becomes clear in the next snapshot [see Fig. 8(c)]. The acoustic impedance of water is much higher than PFH and therefore, as the shock wave crosses from water into the droplet, it converges and focuses at the geometrical focus,

also known as the focal point of the droplet. Here, it is expected that the incoming shock pressure is amplified and reaches a maximum value. The correspondence between the shadowgraphs and the numerical Schlieren is excellent and consistent over multiple shock pressures (15–25 MPa) and droplet radii (600–1000  $\mu\text{m}$ ) considered here.

#### IV. DISCUSSION

In this work, we have obtained the relationship between the shock and particle velocity for PFH by performing planar impact experiments using a single-stage mesoscale gas-launcher. As mentioned in Sec. III, the experimental errors associated with the shock velocity measurements increase at higher impact speeds, where the shock wave is captured in fewer frames and where motion blur effects become more notable within the camera exposure time (100–200 ns). Additionally, in some cases, the container cracks, causing cavitation within the sample, further reducing the available frames for measuring the shock wave speed. For improved measurements of higher shock wave speeds, one could resort to non-optical techniques such as Photon Doppler Velocimetry [55, 56], which would also permit using a sturdier container that could sustain such high impact speeds without breaking, thus preventing cavitation in the liquid. Nevertheless, the experimental errors introduced are considered when fitting the  $u_s - u_p$  curve for PFH, minimizing the bias from higher impact speeds, and thereby ensuring that the kinematic EOS is valid for lower Mach numbers, as seen from the correspondence between our experiments and simulations for both the impact and the shock-droplet experiments.

Aligned with applications of perfluorocarbon droplets for biomedical applications involving acoustic excitation, the EOS has also been validated for a shock wave interacting with a sub-millimetric PFH droplet by using ultra-high-speed shadowgraphy. Here, in the numerical simulations performed, the selected reference speed of sound for PFH is 5% lower than the expected sound speed of  $510.5 \text{ m s}^{-1}$  at  $25 \text{ }^\circ\text{C}$  [47], which is justified by the excellent match between experiments and numerical simulations. A change in the reference sound speed of materials by up to  $\pm 10\%$  is deemed reasonable for low Mach flows,  $M \approx 1 + \beta$ , with  $\beta \ll 1$ , as noted in other shock-interaction numerical studies [21, 57]. The correspondence between experiments and numerical simulations confirms that our fitted NASG EOS is valid at low Mach numbers (here  $M \approx 1$ ).

A comparable NASG EOS could also be fitted by using the derived saturation properties of PFH from the work of Gao *et al.* [20] following the methodology outlined in Le Métayer and Saurel [32]. The EOS obtained in this manner also requires an adjustment in the reference speed of sound at a given temperature to match the corresponding simulations with the experiments described here. This EOS works equivalently well for the shock-droplet case when lower input pressures for the shock wave are used as compared to the intensities tested in this study (with  $M \approx 1$ ). However, it fails to reproduce experimental results at higher input pressures and higher Mach numbers. Therefore, the EOS derived in this study, based on shock compression of PFH, is more robust for higher input pressures.

#### V. CONCLUSION

Perfluorohexane shows promise to be employed as a liquid in biocompatible agents designed for ultrasound and shock wave-based therapies. To study the mechanisms involved in such acoustic-agent interactions, several studies focus on performing numerical research, which requires an EOS specially tuned for high-pressure conditions. In this study, we have performed planar impact experiments using a single-stage mesoscale gas launcher and obtained a relationship between the shock and particle velocity for PFH. The experiments are especially successful for low Mach number flow regimes that can be expected in biomedical applications. This relationship can be used as a precursor to determine other thermodynamic equations of state. Here, we use a well-established multi-objective optimization scheme to determine the necessary constants to define the Noble-Abel Stiffened-Gas (NASG) equation, which is a convex equation of state accounting for agitation and repulsive molecular effects. The equation is then used in hydrodynamic numerical simulations performed using ECOGEN to validate our EOS. We show that we can successfully simulate the shock propagation in our impact and shock-droplet interaction experiments. The provided EOS enables numerical investigations of shock-droplet interactions at micro- and nano-scales, which could help us to better understand the physical mechanisms underlying acoustic waves interaction with biomedical agents. Such studies could be used to improve acoustic driving and agent formulation for biomedical applications, and in particular, accelerate the use of perfluorocarbon droplets as theranostic agents.

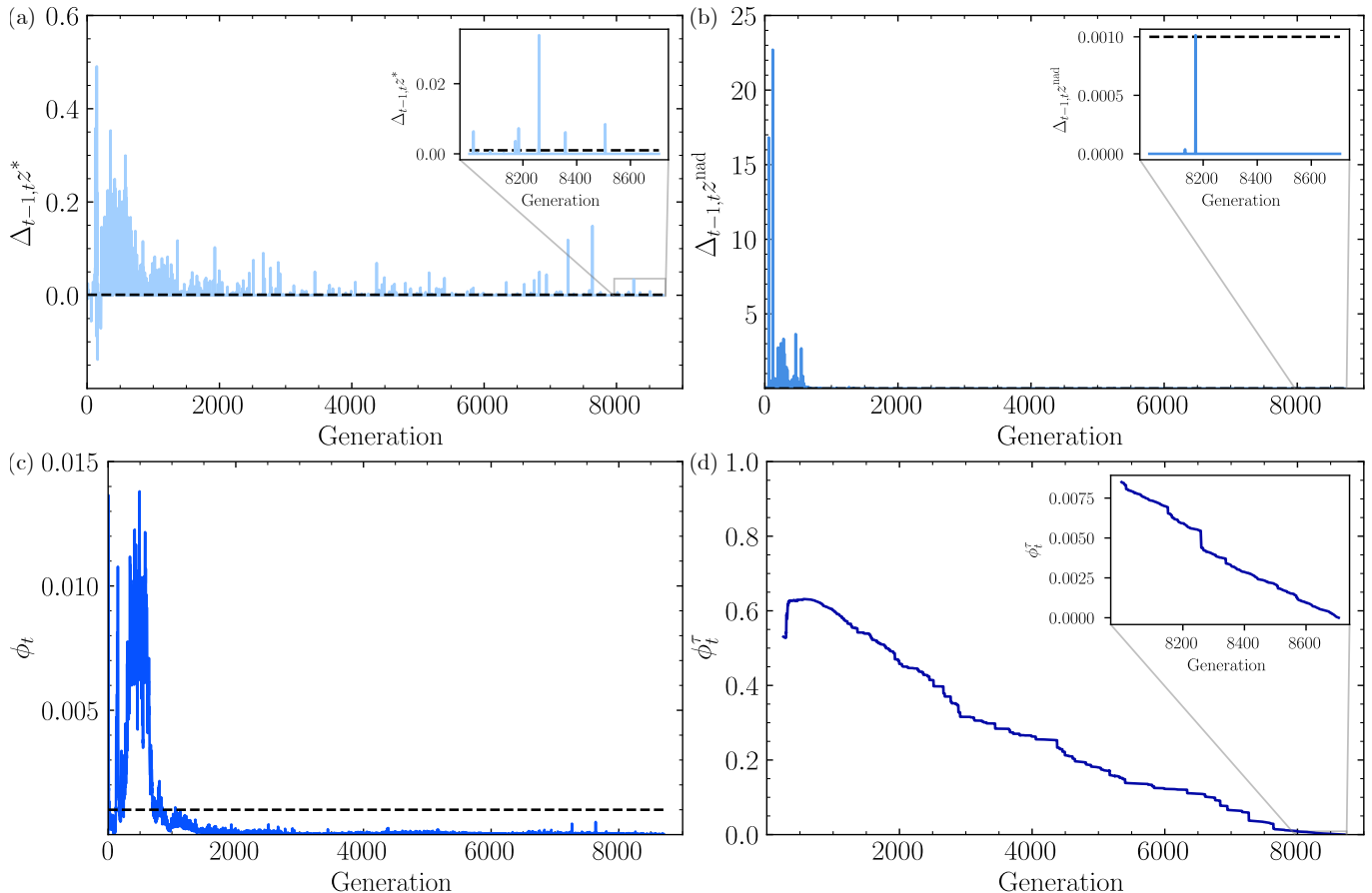


FIG. 9. Evolution of the convergence criteria for determining the NASG EOS parameters for PFH. (a) Normalized change of ideal point,  $\Delta_{t-1,t}z^*$ , (b) Normalized change of nadir point,  $\Delta_{t-1,t}z^{nad}$ , (c) Improvement of normalized IGD over successive generations,  $\phi_t$ . (d) Visualization IGD metric, normalized to the last generation,  $\tau_{end} = 8706$ , plotted for  $250 \leq t_{gen} \leq \tau_{end}$ . The quantity decreases over generations and reaches a sufficiently low value to indicate convergence of the optimization. The dotted black line in (a-c) shows the tolerance ( $\epsilon = 0.001$ ,  $\chi = 100$ ) used as the termination criteria for the optimization run.

## ACKNOWLEDGMENTS

This project was funded by the Swiss National Science Foundation (grant number 200021\_200567). The authors acknowledge ESRF for providing resources to conduct the experiments. The authors would also like to thank Dr. Sayaka Ichihara for helping with the shock-droplet experiments and Mr. Dengel Karakoc from the Techpool facility at ETH Zürich for assisting with the manufacturing process of the sabots and containers.

## Appendix A: Convergence and termination criteria for optimization runs

The convergence of an optimization run is monitored using two steps: (a) convergence to extreme points and (b) convergence of solution diversity [48, 51]. The convergence to extreme points is monitored by computing the normalized change of the ideal (*i.e.*, minimum) and nadir (*i.e.*, maximum) points between successive generations, defined as [51]

$$\Delta_{t-1,t}z^* = \max_{i=1}^M \frac{z_i^*(t-1) - z_i^*(t)}{z_i^{nad}(t) - z_i^*(t)} \quad (A1)$$

$$\Delta_{t-1,t}z^{nad} = \max_{i=1}^M \frac{z_i^{nad}(t-1) - z_i^{nad}(t)}{z_i^{nad}(t) - z_i^*(t)} \quad (A2)$$

where  $z_i^*$  is the realized ideal point and  $z_i^{nad}$  is the realized nadir point for the  $i$ -th objective normalized at time  $t$ . To monitor the diversity enhancement of the solution, a cumulative approach from the initial ( $t = 0$ ) to the current

generation ( $t = \tau$ ) is used. We first determine the normalized  $i$ -th objective value of the  $j$ -th non-dominated point at generation  $t$ ,  $\overline{P}_i^j(t)$ , using the ideal and nadir points at  $t = \tau$ .

$$\overline{P}_i^j(t) = \frac{P_i^j(t) - z_i^*(\tau)}{z_i^{\text{nad}}(\tau) - z_i^*(\tau)} \quad (\text{A3})$$

The improvement of the Inverted Generational Distance (IGD) metric between the normalized solution values between two successive generations is evaluated as defined below

$$\begin{aligned} \phi_t &= \text{IGD}(\overline{P}_i^t(t-1), \overline{P}_i^t(t)) \\ &= \frac{1}{|\overline{P}_i^t(t)|} \sum_{i=1}^{|\overline{P}_i^t(t)|} \left( \min_{j=1}^{|\overline{P}_i^t(t-1)|} \|\overline{P}_i^t(t) - \overline{P}_i^t(t-1)\| \right) \end{aligned} \quad (\text{A4})$$

Eq. (A4) provides a good estimate of the broadening of the obtained solutions in successive generations. As a termination criterion, we ensure that the three quantities determined by Eqs. (A1), (A2), and (A4) are below a certain tolerance,  $\epsilon$ , over a given number of transitions, by using a sliding window,  $\chi$  [51]. For example, for a multi-objective optimization run of PFH, we set a tolerance of  $\epsilon = 0.001$  and use a window size of  $\chi = 100$ . This implies that a run is found to be “complete” if  $\Delta_{t-1,t}z^*$ ,  $\Delta_{t-1,t}z^{\text{nad}}$  and  $\phi_t$  vary by less than 0.1% over the last 100 generational transitions of the run. To visualize the convergence, it is beneficial to renormalize Eq. (A4) over the complete interval  $0 \leq t \leq \tau_{\text{end}}$  and evaluate the new IGD metric as given below

$$\phi_t^\tau = \text{IGD}(\overline{P}_i^{\tau_{\text{end}}}(t), \overline{P}_i^{\tau_{\text{end}}}(\tau_{\text{end}})) \quad (\text{A5})$$

While Eq. (A5) can be reevaluated every  $\chi$  generations to effectively monitor convergence, this method has a high computational overhead due to the requirement of renormalizing the solution every  $\chi$  generations. Hence, Eq. (A5) is only used as a visualization tool, while the termination is set by Eqs. (A1), (A2) and (A4) [51]. Fig. 9 plots  $\Delta_{t-1,t}z^*$ ,  $\Delta_{t-1,t}z^{\text{nad}}$ ,  $\phi_t$  and  $\phi_t^\tau$  for one of the optimization runs. As depicted, all quantities are well below the set tolerance value of  $\epsilon = 0.001$ , for at least  $\chi = 100$  generations, with  $\phi_t^\tau$  continuously decreasing over time, indicating that the optimization has converged and can be terminated.

## Appendix B: Uncertainty quantification of experimental data

Experimental errors are quantified in a manner described previously for such experiments by Mitchell and Nellis [58]. Briefly, an error in impact-related quantities propagates throughout the calculation due to the flyer EOS being used to determine the properties of the liquid. Using a Monte-Carlo estimate of error propagation, for the pressure and the specific volume in Eq. (1) this corresponds to

$$\begin{aligned} \frac{\delta P}{P} &= \left[ \left( \frac{\delta \rho_0}{\rho_0} \right)^2 + \left( \frac{\delta u_s}{u_s} \right)^2 + \left( \frac{\delta u_p}{u_p} \right)^2 \right]^{1/2} \\ \frac{\delta v}{v} &= \left[ \left( \frac{\delta \rho_0}{\rho_0} \right)^2 + (\eta - 1)^2 \left\{ \left( \frac{\delta u_s}{u_s} \right)^2 + \left( \frac{\delta u_p}{u_p} \right)^2 \right\} \right]^{1/2} \end{aligned} \quad (\text{B1})$$

where  $\eta = \rho/\rho_0$  is the compression factor, and the other terms are as defined previously. For the internal energy, a simple estimate can be obtained for the error by setting  $P_0 = 0$ , giving the error as  $\delta e/e = 2\delta u_p/u_p$ . For the flyer, we use  $\delta u_p/u_p \approx \delta u_f/u_f$ . This has a minor error contribution since the laser gates are well-calibrated and the sampling rate of the oscilloscope is sufficient to accurately measure the impact speed.

To determine the particle velocity in the container during impact, we include the 2% error in the EOS of PMMA as estimated by Jordan *et al.* [43] in their experiments. This introduces a systematic error in the evaluation of the flyer and the container pressures, and the uncertainty in particle velocity is taken as  $\delta u_p = \frac{1}{2}|u_{p,c,\text{max}} - u_{p,c,\text{min}}|$ , where  $u_{p,c,\text{max}}$  is obtained by the intersection of  $P_{c,\text{min}}$  and  $P_{f,\text{max}}$ , and  $u_{p,c,\text{min}}$  is obtained by the intersection of  $P_{c,\text{max}}$  and  $P_{f,\text{min}}$ . The two extrema of the expected particle velocities are used to calculate the possible bounds of the release adiabats in the  $P - u_p$  plane, where an additional error is introduced by the term  $du_s/du_p$  in the Riemann integral.

The largest error contribution arises from the measurement of the shock velocity from the images,  $\delta u_{s,1}/u_{s,1}$ , especially at higher speeds. The shock velocity is estimated as  $u_s = \Delta x/\Delta t$ , where  $\Delta x$  is the distance travelled between

two frames having an interval of  $\Delta t$ . The error in the shock velocity estimation is taken as

$$\frac{\delta u_{s,1}}{u_{s,1}} = \left[ \left( \frac{\delta(\Delta x)}{\Delta x} \right)^2 + \left( \frac{\delta(\Delta t)}{\Delta t} \right)^2 \right]^{1/2} \quad (\text{B2})$$

where  $\delta(\Delta x)$  is the uncertainty associated with the edge detection of the shock front and  $\delta(\Delta t)$  is evaluated by taking a two-standard deviation interframe window [59].

Finally, the error on the liquid particle velocity is evaluated in a similar fashion to the container particle velocity,  $\delta u_{p,l} = \frac{1}{2}|u_{p,l,\max} - u_{p,l,\min}|$ , where  $u_{p,l,\max}$  is obtained by the intersection of  $P_{l,\max} \propto \rho_{\text{PFH},\max}(u_{s,1} + \delta u_{s,1})$  and the release adiabat evaluated from  $u_{p,c,\max}$ , and  $u_{p,l,\min}$  is obtained by the intersection of  $P_{l,\min} \propto \rho_{\text{PFH},\min}(u_{s,1} - \delta u_{s,1})$  and the release isentrope evaluated from  $u_{p,c,\min}$ . Then, the errors on the thermodynamic quantities are evaluated using Eq. (B1).

- 
- [1] G. Shakya, M. Cattaneo, G. Guerriero, A. Prasanna, S. Fiorini, and O. Supponen, Ultrasound-responsive microbubbles and nanodroplets: A pathway to targeted drug delivery, *Advanced Drug Delivery Reviews* **206**, 10.1016/j.addr.2023.115178 (2024).
  - [2] K. C. Lowe, Fluorinated blood substitutes and oxygen carriers, *Journal of Fluorine Chemistry* **109**, 59 (2001).
  - [3] G. Picheth, S. Houvenagel, C. Dejean, O. Couture, R. Alves de Freitas, L. Moine, and N. Tsapis, Echogenicity enhancement by end-fluorinated polylactide perfluorohexane nanocapsules: Towards ultrasound-activable nanosystems, *Acta Biomaterialia* **64**, 313 (2017).
  - [4] O. D. Kripfgans, J. B. Fowlkes, D. L. Miller, O. P. Eldevik, and P. L. Carson, Acoustic droplet vaporization for therapeutic and diagnostic applications, *Ultrasound in Med. & Biol.* **26**, 1177 (2000).
  - [5] R. Díaz-López, N. Tsapis, and E. Fattal, Liquid perfluorocarbons as contrast agents for ultrasonography and  $^{19}\text{F}$ -MRI, *Pharmaceutical Research* **27**, 1 (2010).
  - [6] A. V. Namen, S. Jandhyala, T. Jordan, and G. P. Luke, Repeated Acoustic Vaporization of Perfluorohexane Nanodroplets for Contrast-Enhanced Ultrasound Imaging, *IEEE Transactions on Ultrasonics, Ferroelectrics, and Frequency Control* **68**, 3497 (2021).
  - [7] Q. Zeng, L. Qiao, L. Cheng, C. Li, Z. Cao, Z. Chen, Y. Wang, and J. Liu, Perfluorohexane-Loaded Polymeric Nanovesicles with Oxygen Supply for Enhanced Sonodynamic Therapy, *ACS Biomaterials Science and Engineering* **6**, 2956 (2020).
  - [8] H. Xiao, M. Aliabouzar, and M. L. Fabiilli, Acoustically responsive scaffolds: Unraveling release kinetics and mechanisms for sustained, steady drug delivery, *Journal of Controlled Release* **374**, 205 (2024).
  - [9] M. A. Borden, G. Shakya, A. Upadhyay, and K. H. Song, Acoustic nanodrops for biomedical applications, *Current Opinion in Colloid and Interface Science* **50**, 10.1016/j.cocis.2020.08.008 (2020).
  - [10] H. Maeda, Toward a full understanding of the EPR effect in primary and metastatic tumors as well as issues related to its heterogeneity, *Advanced Drug Delivery Reviews* **91**, 3 (2015).
  - [11] O. Shpak, M. Verweij, H. J. Vos, N. De Jong, D. Lohse, and M. Versluis, Acoustic droplet vaporization is initiated by superharmonic focusing, *Proceedings of the National Academy of Sciences of the United States of America* **111**, 10.1073/pnas.1312171111 (2014).
  - [12] S. Fiorini, A. Prasanna, G. Shakya, M. Cattaneo, and O. Supponen, Positive pressure matters in acoustic droplet vaporization, arXiv:2407.16455 <https://doi.org/10.48550/arXiv.2407.16455> (2024).
  - [13] A. M. Loske, *Medical and biomedical applications of shock waves* (Springer, 2017).
  - [14] M. Maier, B. Averbeck, S. Milz, H. J. Refior, and C. Schmitz, Substance p and prostaglandin e<sub>2</sub> release after shock wave application to the rabbit femur, *Clinical Orthopaedics and Related Research* **406**, 237 (2003).
  - [15] R. Beisteiner, E. Matt, C. Fan, H. Baldysiak, M. Schönfeld, T. Philippi Novak, A. Amini, T. Aslan, R. Reinecke, J. Lehrner, *et al.*, Transcranial pulse stimulation with ultrasound in alzheimer’s disease—a new navigated focal brain therapy, *Advanced Science* **7**, 1902583 (2020).
  - [16] T. Kisch, W. Wuerfel, V. Forstmeier, E. Liodaki, F. H. Stang, K. Knobloch, P. Mailaender, and R. Kraemer, Repetitive shock wave therapy improves muscular microcirculation, *Journal of Surgical Research* **201**, 440 (2016).
  - [17] F. Marano, M. Argenziano, R. Frairia, A. Adamini, O. Bosco, L. Rinella, N. Fortunati, R. Cavalli, and M. G. Catalano, Doxorubicin-loaded nanobubbles combined with extracorporeal shock waves: basis for a new drug delivery tool in anaplastic thyroid cancer, *Thyroid* **26**, 705 (2016).
  - [18] F. Marano, R. Frairia, L. Rinella, M. Argenziano, B. Bussolati, C. Grange, R. Mastrocola, I. Castellano, L. Berta, R. Cavalli, *et al.*, Combining doxorubicin-nanobubbles and shockwaves for anaplastic thyroid cancer treatment: preclinical study in a xenograft mouse model, *Endocrine-related cancer* **24**, 275 (2017).
  - [19] R. Menikoff and B. J. Plohr, The Riemann problem for fluid flow of real materials, *Reviews of Modern Physics* **61**, 75 (1988).
  - [20] K. Gao, A. Köster, M. Thol, J. Wu, and E. W. Lemmon, Equations of State for the Thermodynamic Properties of n-Perfluorobutane, n-Perfluoropentane, and n-Perfluorohexane, *Industrial and Engineering Chemistry Research* **60**, 17207 (2021).

- [21] J. P. Cocchi, R. Saurel, and J. C. Loraud, Treatment of interface problems with Godunov-type schemes, *Shock Waves* **5**, 347 (1996).
- [22] M. H. Rice and J. M. Walsh, Equation of state of water to 250 kilobars, *The Journal of Chemical Physics* **26**, 824 (1957).
- [23] L. M. Barker and R. E. Hollenbach, Shock-wave studies of PMMA, fused silica, and sapphire, *Journal of Applied Physics* **41**, 4208 (1970).
- [24] W. J. Nellis and A. C. Mitchell, Shock compression of liquid argon, nitrogen, and oxygen to 90 GPa (900 kbar), *The Journal of Chemical Physics* **73**, 6137 (1980).
- [25] A. C. Mitchell and W. J. Nellis, Equation of state and electrical conductivity of water and ammonia shocked to the 100 GPa (1 Mbar) pressure range, *The Journal of Chemical Physics* **76**, 6273 (1981).
- [26] W. J. M. Rankine, XV. On the thermodynamic theory of waves of finite longitudinal disturbance, *Phil. Trans. R. Soc.* , 277 (1870).
- [27] H. Hugoniot, Mémoire sur la propagation du mouvement dans un fluide indéfini (première partie), *Journal de l'Ecole Polytechnique* , 3 (1887).
- [28] R. Saurel, F. Petitpas, and R. Abgrall, Modelling phase transition in metastable liquids: Application to cavitating and flashing flows, *Journal of Fluid Mechanics* **607**, 313 (2008).
- [29] G. A. Cox and M. A. Christie, Fitting of a multiphase equation of state with swarm intelligence, *Journal of Physics Condensed Matter* **27**, 10.1088/0953-8984/27/40/405201 (2015).
- [30] P. C. Myint, L. X. Benedict, C. J. Wu, and J. L. Belof, Minimization of Gibbs Energy in High-Pressure Multiphase, Multicomponent Mixtures through Particle Swarm Optimization, *ACS Omega* **6**, 13341 (2021).
- [31] G. Robert, V. Dubois, and P. Legrand, Using maximum likelihood estimation approach to adjust parameters of multiphase equations of state: Molybdenum as an example, *Journal of Applied Physics* **131**, 10.1063/5.0081299 (2022).
- [32] O. Le Métayer and R. Saurel, The Noble-Abel Stiffened-Gas equation of state, *Physics of Fluids* **28**, 10.1063/1.4945981 (2016).
- [33] M. E. Rutherford, D. J. Chapman, J. G. Derrick, J. R. Patten, P. A. Bland, A. Rack, G. S. Collins, and D. E. Eakins, Probing the early stages of shock-induced chondritic meteorite formation at the mesoscale, *Scientific Reports* **7**, 10.1038/srep45206 (2017).
- [34] A. Rack, B. Lukić, D. J. Chapman, J. Strucka, Y. Yao, K. Mughal, D. Maler, S. Efimov, O. Belozerov, Y. Krasik, J. P. Chittenden, S. N. Bland, A. Sollier, G. C. Ganzenmüller, A. Cohen, D. Levi-Hevroni, W. G. Proud, P. Song, and D. E. Eakins, Dynamic loading platforms coupled to ultra-high speed X-ray imaging at beamline ID19 of the European Synchrotron ESRF, *High Pressure Research* **44**, 400 (2024).
- [35] G. T. Bokman, L. Biasiori-Poulanges, D. W. Meyer, and O. Supponen, Scaling laws for bubble collapse driven by an impulsive shock wave, *Journal of Fluid Mechanics* **967**, 10.1017/jfm.2023.514 (2023).
- [36] K. Schmidmayer, F. Petitpas, S. Le Martelot, and É. Daniel, ECOGEN: An open-source tool for multiphase, compressible, multiphysics flows, *Computer Physics Communications* **251**, 107093 (2020).
- [37] T. Trummler, S. H. Bryngelson, K. Schmidmayer, S. J. Schmidt, T. Colonius, and N. A. Adams, Near-surface dynamics of a gas bubble collapsing above a crevice, *Journal of Fluid Mechanics* **899**, A16 (2020).
- [38] B. Dorschner, L. Biasiori-Poulanges, K. Schmidmayer, H. El-Rabii, and T. Colonius, On the formation and recurrent shedding of ligaments in droplet aerobreakup, *Journal of Fluid Mechanics* **904**, 10.1017/jfm.2020.699 (2020).
- [39] G. T. Bokman, L. Biasiori-Poulanges, B. Lukić, K. Schmidmayer, C. Bourquard, E. Baumann, A. Rack, B. J. Olson, and O. Supponen, Impulse-driven release of gas-encapsulated drops, *Journal of Fluid Mechanics* **1001**, 10.1017/jfm.2024.1124 (2024).
- [40] A. K. Kapila, R. Menikoff, J. B. Bdzil, S. F. Son, and D. S. Stewart, Two-phase modeling of deflagration-to-detonation transition in granular materials: Reduced equations, *Physics of Fluids* **13**, 3002 (2001).
- [41] Richard Saurel, F. Petitpas, and R. A. Berry, Simple and efficient relaxation methods for interfaces separating compressible fluids, cavitating flows and shocks in multiphase mixtures, *Journal of Computational Physics* **228**, 1678 (2009).
- [42] O. Le Métayer, J. Massoni, and R. Saurel, Élaboration des lois d'état d'un liquide et de sa vapeur pour les modèles d'écoulements diphasiques, *International Journal of Thermal Sciences* **43**, 265 (2004).
- [43] J. L. Jordan, D. Casem, and M. Zellner, Shock Response of Polymethylmethacrylate, *Journal of Dynamic Behavior of Materials* **2**, 372 (2016).
- [44] H. Kleine, H. Grönig, and K. Takayama, Simultaneous shadow, schlieren and interferometric visualization of compressible flows, *Optics and Lasers in Engineering* **44**, 170 (2006).
- [45] J. H. Gladstone and T. Dale, XIV. Researches on the refraction, dispersion, and sensitiveness of liquids, *Phil. Trans. R. Soc.* **153**, 317 (1863).
- [46] T. Ahrens, Equation of State, in *High-Pressure Shock Compression of Solids* (Springer New York, NY, 1993) pp. 75–113.
- [47] J. N. Marsh, C. S. Hall, S. A. Wickline, and G. M. Lanza, Temperature dependence of acoustic impedance for specific fluorocarbon liquids, *The Journal of the Acoustical Society of America* **112**, 2858 (2002).
- [48] J. Blank and K. Deb, Pymoo: Multi-Objective Optimization in Python, *IEEE Access* **8**, 89497 (2020).
- [49] K. Deb, A. Pratap, S. Agarwal, and T. Meyarivan, A Fast and Elitist Multiobjective Genetic Algorithm: NSGA-II, *IEEE Transactions on Evolutionary Computation* **6** (2002).
- [50] K. Deb, K. Sindhya, and T. Okabe, Self-adaptive simulated binary crossover for real-parameter optimization, in *Proceedings of the 9th Annual Conference on Genetic and Evolutionary Computation* (ACM Digital Library, 2007) pp. 1187–1194.
- [51] J. Blank and K. Deb, A Running Performance Metric and Termination Criterion for Evaluating Evolutionary Multi-and Many-objective Optimization Algorithms, in *2020 IEEE Congress on Evolutionary Computation (CEC)* (2020) pp. 1–8.

- [52] P. T. Boggs and J. E. Rogers, Orthogonal distance regression, in *Statistical analysis of measurement error models and applications: proceedings of the AMS-IMS-SIAM joint summer research conference held June 10-16, 1989*, Vol. 112 (1990) p. 186.
- [53] NIST, Poly(methyl methacrylate).
- [54] A. P. Wierzbicki, The use of reference objectives in multiobjective optimization, in *Multiple Criteria Decision Making Theory and Application. Lectures in Economics and Mathematical Systems*, Vol. 177, edited by G. Fandel and T. Gal (Springer, Berlin, Heidelberg, 1980).
- [55] D. H. Dolan, Extreme measurements with Photonic Doppler Velocimetry (PDV), *Review of Scientific Instruments* **91**, 10.1063/5.0004363 (2020).
- [56] V. Kilic, C. S. DiMarco, J. M. Diamond, P. Chu, K. T. Ramesh, Z. Wang, and M. A. Foster, Time Lens Photon Doppler Velocimetry (TL-PDV) for extreme measurements, *Nature Communications* **15**, 10.1038/s41467-024-52094-y (2024).
- [57] E. Johnsen and T. Colonius, Shock-induced collapse of a gas bubble in shockwave lithotripsy, *The Journal of the Acoustical Society of America* **124**, 2011 (2008).
- [58] A. C. Mitchell and W. J. Nellis, Shock compression of aluminum, copper, and tantalum, *Journal of Applied Physics* **52**, 3363 (1981).
- [59] A. Possolo, *Simple Guide for Evaluating and Expressing the Uncertainty of NIST Measurement Results*, Tech. Rep. (National Institute of Standards and Technology, Gaithersburg, MD, 2015).